# A residual-based stabilized finite element formulation for incompressible flow problems in the Arlequin framework

Jeferson Wilian Dossa Fernandes, Andrea Barbarulo, Hachmi Ben Dhia, Rodolfo André Kuche Sanches

# A residual-based stabilized finite element formulation for incompressible flow problems in the Arlequin framework

Jeferson Wilian Dossa Fernandes[a,*], Andrea Barbarulo[b], Hachmi Ben Dhia[b], Rodolfo André Kuche Sanches[a]

[a] *University of São Paulo, School of Engineering of São Carlos, Structural Engineering Department, Av. Trabalhador Sãocarlense, 400, São Carlos, São Paulo, Brazil*
[b] *Laboratoire MSSMat, CentraleSupélec/CNRS UMR 8579/ Université Paris Saclay, 91190 Gif-sur-Yvette, France*

**Abstract**

Many fluid flow problems involve localized effects within a larger flow domain, with boundary layers close to solid boundaries being one of the most common. Accurate and realistic computational analysis of such problems requires that the local flow behavior is properly represented by a numerical formulation with affordable computational cost. Among several strategies developed in the computational mechanics to deal with multiscale phenomena, the Arlequin method proposes overlapping a local discretization to a global one and gluing both models by Lagrange multipliers field, being successful in the solid mechanics context, but unexplored for CFD analysis. In this work, we introduce the Arlequin method to the numerical analysis of unsteady incompressible flows. Differently from the previous works involving incompressible media, a stabilized finite element formulation is employed. To improve stability and conditioning of the algebraic system of equations, we propose a novel Residual-Based Stabilized Arlequin Formulation. The resulting formulation is tested in various numerical examples, considering structured and unstructured, coincident and non-coincident finite element discretization, Stokes problems and convection dominated Navier-Stokes problems, steady and transient cases, showing the methodology precision and robustness.

*Keywords:* Computational Fluid Dynamics, Multiscale Analysis, Arlequin Method, Stabilized Finite Elements

## 1. Introduction

Several fluid dynamics problems involve multiscale effects due to many aspects. The most common is the boundary layer effects near immersed solids. Regarding numerical analysis, such problem remains a challenge, stimulating the development of several computational techniques in the last decades.

Many researchers have concentrated efforts to develop alternatives for the simulation of multiscale problems. Among them, one can mention the Variational Multiscale Methods [1] and the partition of unity-based methods [2], including the Generalized [3] and Extended [4] versions of the Finite Element Method.

A convenient way of dealing with multiscale analysis in complex geometries consists in overlapping

*Corresponding author
*Email address:* jefersondossa@usp.br (Jeferson Wilian Dossa Fernandes)

discretization techniques. In the past decades, many different methods have been developed for this purpose as the $S$ [5, 6], Chimera [7, 8] and Arlequin [9, 10] methods.

The Arlequin method, introduced by [9], unlike other multiscale methods, has its basis on the superposition of local models, with a finite element discretization able to capture the localized effects, to the global computational model. This technique has been applied to the solution of many engineering problems, including crack propagation [11], contact and impact [12, 13], atomic-to-continuum coupling [14, 15], stochastic analysis [16] and more recently the Arlequin method has been combined to reduced order models [17, 18].

Although the Arlequin method remains unexplored on the fluid dynamics context, Jamond and Ben Dhia [19] performed a broad analysis of this methodology applied to incompressible materials employing Taylor-Hood stable finite elements. In such work, many parameters of the Arlequin framework are investigated and, in summary, the bigger drawback observed concerns in circumventing the LBB condition, as only some of the tested combinations were shown as stable.

On the other side, as shown by Ben Dhia and Rateau [20] and [21], for the Arlequin method to be successful, some parameters such as a coupling zone and operator, as well as an energy weighting function, need to be chosen properly. Regarding the coupling operator, for example, its definition affects directly the numerical solution quality and the algebraic system conditioning. The most common choices are the $L^2$ and $H^1$ coupling operators, presented in details by Ben Dhia and Rateau [20], Guidault and Belytschko [21]. The $L^2$ operator provides a continuous solution, in a weak sense, while the $H^1$ coupling operator ensures the continuity of a linear combination between the variable coupled and its Laplacian, based on specified coupling constants [21]. Moreover, $H^1$ coupling operator gives the algebraic system a better conditioning [10].

As an extension of the Arlequin method developments in the context of Navier-Stokes incompressible flows, in this paper we propose a residual based stabilized methodology using equal order mixed pressure-velocity finite elements for both local and global domains, completely circumventing the LBB condition drawbacks. In order to do so, in both models, we employ the pressure-stabilizing/Petrov-Galerkin (PSPG) method [22], which is the Navier-Stokes version of the pressure stabilization given in [23] for Stokes flow.

The use of $L^2$ coupling operator in the context of incompressible flows can easily result into an oscillating Lagrange multipliers field. In order to ensure a stable solution, we propose to add a new residual-based stabilization term to the coupling equation. The new stabilization ensures a better conditioning to the algebraic system and also allows the use of local model space of functions for the coupling operator in a stable way.

This paper is organized as follows: section 2 presents the stabilized incompressible flow problem considering a single scale model. In Section 3 we present general aspects of the Arlequin framework and develop the technique for solving incompressible flow problems. Following, in section 5.1 the proposed formulation is applied for the Stokes problem and extended to the incompressible Navier-Stokes equations in section 5.2. Numerical examples are presented in both sections 5.1 and 5.2. Finally, concluding remarks are drawn in Section 7.

## 2. Stabilized Navier-Stokes Solution - Monomodel problem

### *2.1. Governing equations*

Incompressible isothermal Newtonian flows in a computational domain $\Omega$, at time $t \in (0, T)$, are governed by momentum and continuity equations, given by:

$$\rho\left(\frac{\partial \mathbf{u}}{\partial t} + \mathbf{u}\cdot\nabla\mathbf{u} - \mathbf{f}\right) - \nabla\cdot\boldsymbol{\sigma} = \mathbf{0} \tag{1}$$

and

$$\nabla\cdot\mathbf{u} = 0, \tag{2}$$

where $\rho$, $\mathbf{f}$, $\mathbf{u}$ and $\boldsymbol{\sigma}$ are respectively the fluid density, body force, velocity and the Cauchy stress tensor. For Newtonian incompressible flows $\boldsymbol{\sigma}$ is expressed by the constitutive equation:

$$\boldsymbol{\sigma}(\mathbf{u}, p) = -p\mathbf{I} + 2\mu\boldsymbol{\varepsilon}(\mathbf{u}), \tag{3}$$

where $p$ being the pressure, $\mathbf{I}$ is the identity tensor, $\mu$ the dynamic viscosity and the strain rate $\boldsymbol{\varepsilon}(\mathbf{u}) = \left(\nabla\mathbf{u} + \nabla\mathbf{u}^T\right)/2$.

To finish the problem statement, boundary and initial conditions must be considered. For instance, the initial velocity field $\mathbf{u}_I$ is required to be divergence-free, i.e., $\nabla\cdot\mathbf{u}_I = 0$. Moreover, Dirichlet ($\mathbf{u}_D$) and Neumann, or traction ($\mathbf{h}$), boundary conditions are applied on portions $\Gamma_D$ and $\Gamma_t$, respectively, of the computational domain boundary $\Gamma$.

### *2.2. Weak form and finite elements spatial discretization*

To get a variational formulation with finite elements discretization let us define, over the computational domain $\Omega$, the finite dimensional trial solution function spaces $\mathcal{S}_u^h$ and $\mathcal{S}_p^h$, and the finite dimensional weighting (or test) function spaces $\mathcal{V}_u^h$ and $\mathcal{V}_p^h$, being the indexes $u$ and $p$ respectively related to velocity and pressure fields, as

$$\mathcal{S}_u^h = \left\{\mathbf{u}^h | \mathbf{u}^h(\cdot, t) \in H^{1h}(\Omega), \mathbf{u}^h \doteq \mathbf{u}_D^h \text{ on } \Gamma_D\right\}, \tag{4}$$

$$\mathcal{S}_p^h = \left\{p^h | p^h(\cdot) \in L^{2h}(\Omega), \int_\Omega p^h \, d\Omega = 0 \text{ if } \Gamma = \Gamma_D\right\}, \tag{5}$$

$$\mathcal{V}_u^h = \left\{\mathbf{w}^h | \mathbf{w}^h(\cdot) \in H^{1h}(\Omega), \mathbf{w}^h \doteq \mathbf{0} \text{ on } \Gamma_D\right\}, \tag{6}$$

$$\mathcal{V}_p^h = \mathcal{S}_p^h. \tag{7}$$

where the superscript $h$ denotes the related finite element interpolation.

However, it is well known that such equations present restrictions to the direct application of Galerkin method, as the convective terms can produce spurious variations and the choice of pressure trial and test space is subjected to the Ladyzhenskaya–Babuška–Brezzi (LBB) conditions [24] in order to ensure a stable solution. Both instabilities are suppressed by means of the adopted residual-based formulation Brooks and Hughes [25], Hughes et al. [23], Tezduyar [22, 26], Hsu et al. [27], Bazilevs et al. [28], more specifically,

the method given in [26]. The method cosists of the application of Streamline-Upwind/Petrov-Galerkin (SUPG), Pressure-Stabilized/Petrov-Galerkin (PSGP) and Least-Squares in the Incompressibility Constraint (LSIC) stabilizations as one can see in the mentioned papers.

Applying the weighted residual method to equations (1) and (2), together with the previously mentioned stabilizations and the divergence theorem to the stress component, the stabilized incompressible fluid flow problem can be stated as: find $\left(\mathbf{u}^h, p^h\right) \in \mathcal{S}_u^h \times \mathcal{S}_p^h$ such that $\forall \left(\mathbf{w}^h, q^h\right) \in \mathcal{V}_u^h \times \mathcal{V}_p^h$,

$$\begin{aligned}\int_\Omega \mathbf{w}^h \cdot \rho \left( \frac{\partial \mathbf{u}^h}{\partial t} + \mathbf{u}^h \cdot \nabla \mathbf{u}^h - \mathbf{f}^h \right) \, d\Omega \; + \; \int_\Omega \boldsymbol{\varepsilon}\left(\mathbf{w}^h\right) : \boldsymbol{\sigma}\left(\mathbf{u}^h, p^h\right) \, d\Omega - \int_{\Gamma_t} \mathbf{w}^h \cdot \mathbf{h}^h \, d\Gamma \\ + \sum_{e=1}^{n_{\mathrm{el}}} \int_{\Omega^e} \tau_{\mathrm{SUPG}} \left(\mathbf{u}^h \cdot \nabla \mathbf{w}^h\right) \cdot \mathbf{r}_{\mathrm{M}}\left(\mathbf{u}^h, p^h\right) \, d\Omega + \sum_{e=1}^{n_{\mathrm{el}}} \int_{\Omega^e} \nu_{\mathrm{LSIC}} \nabla \cdot \mathbf{w}^h r_{\mathrm{C}}\left(\mathbf{u}^h\right) \, d\Omega = 0,\end{aligned} \tag{8}$$

and

$$\int_\Omega q^h \nabla \cdot \mathbf{u}^h \, d\Omega + \sum_{e=1}^{n_{\mathrm{el}}} \int_{\Omega^e} \tau_{\mathrm{PSPG}} \left( \frac{\nabla q^h}{\rho} \right) \cdot \mathbf{r}_{\mathrm{M}}\left(\mathbf{u}^h, p^h\right) \, d\Omega = 0, \tag{9}$$

where $n_{\mathrm{el}}$ is the number of finite elements in the domain, $\mathbf{r}_{\mathrm{M}}\left(\mathbf{u}^h, p^h\right)$ and $r_{\mathrm{C}}\left(\mathbf{u}^h\right)$ are the residual of the momentum and continuity equations, respectively, given by

$$\mathbf{r}_{\mathrm{M}}\left(\mathbf{u}^h, p^h\right) = \rho \left( \frac{\partial \mathbf{u}^h}{\partial t} + \mathbf{u}^h \cdot \nabla \mathbf{u}^h - \mathbf{f}^h \right) - \nabla \cdot \boldsymbol{\sigma}\left(\mathbf{u}^h, p^h\right), \tag{10}$$

$$r_{\mathrm{C}}\left(\mathbf{u}^h\right) = \nabla \cdot \mathbf{u}^h. \tag{11}$$

The stabilization parameters $\tau_{\mathrm{SUPG}}$, $\tau_{\mathrm{PSPG}}$ and $\nu_{\mathrm{LSIC}}$, are from [26] and [28]. They are designed to provide a discrete stable and optimally convergent solution under mesh refinement, and are given as

$$\tau_{\mathrm{SUPG}} = \tau_{\mathrm{PSPG}} = \left( \frac{1}{\tau_{\mathrm{SUGN1}}^2} + \frac{1}{\tau_{\mathrm{SUGN2}}^2} + \frac{1}{\tau_{\mathrm{SUGN3}}^2} \right)^{-\frac{1}{2}}, \tag{12}$$

$$\nu_{\mathrm{LSIC}} = \tau_{\mathrm{SUPG}} \left\| \mathbf{u}^h \right\|^2, \tag{13}$$

with

$$\tau_{\mathrm{SUGN1}} = \left( \sum_{i=1}^{n_{\mathrm{en}}} \left| \mathbf{u}^h \cdot \nabla N_i \right| \right)^{-1}, \tag{14}$$

$$\tau_{\mathrm{SUGN2}} = \frac{\Delta t}{2}, \tag{15}$$

$$\tau_{\mathrm{SUGN3}} = \frac{h_{\mathrm{RGN}}^2}{4\nu}, \tag{16}$$

$$h_{\mathrm{RGN}} = 2 \left( \sum_{i=1}^{n_{\mathrm{en}}} \left| \mathbf{r} \cdot \nabla N_i \right| \right)^{-1} \text{ and} \tag{17}$$

$$\mathbf{r} = \frac{\nabla \left| \mathbf{u}^h \right|}{\left\| \nabla \left| \mathbf{u}^h \right| \right\|}, \tag{18}$$

where $n_{\text{en}}$ is the number of element nodes, $\Delta t$ is the time step size, $\nu = \mu/\rho$ the kinematic viscosity and $N_i$ is the $i-th$ shape function.

Equations (8) and (9) can be written in a more compact way as

$$\begin{aligned}\left(\mathbf{w}^h, \rho\frac{\partial \mathbf{u}^h}{\partial t}\right)_\Omega + \left(\boldsymbol{\varepsilon}(\mathbf{w}^h), 2\mu\boldsymbol{\varepsilon}(\mathbf{u}^h)\right)_\Omega + \left(\rho\mathbf{u}^h; \mathbf{w}^h, \nabla\mathbf{u}^h\right)_\Omega - \left(p^h, \nabla\cdot\mathbf{w}^h\right)_\Omega \\ + \left(\tau_{\text{SUPG}}\mathbf{u}^h\cdot\nabla\mathbf{w}^h, \mathbf{r}_{\text{M}}\right)_\Omega + \left(\nu_{\text{LSIC}}\nabla\cdot\mathbf{w}^h, r_{\text{C}}\right)_\Omega = \left(\mathbf{w}^h, \rho\mathbf{f}^h\right)_\Omega + \left(\mathbf{w}^h, \mathbf{h}^h\right)_{\Gamma_t},\end{aligned} \tag{19}$$

$$\left(q^h, \nabla\cdot\mathbf{u}^h\right)_\Omega + \left(\tau_{\text{PSPG}}\frac{\nabla q^h}{\rho}, \mathbf{r}_{\text{M}}\right)_\Omega = 0, \tag{20}$$

where the convection term represented by a trilinear form is given by

$$\left(\rho\mathbf{u}^h; \mathbf{w}^h, \mathbf{u}^h\right) = \int_\Omega \rho\mathbf{w}^h\cdot\left(\mathbf{u}^h\cdot\nabla\right)\mathbf{u}^h\, d\Omega, \tag{21}$$

The resulting nonlinear system (19)-(20) can also be represented in a matrix form as

$$\mathbf{M}\dot{\mathbf{U}} + \mathbf{K}(\mathbf{U})\mathbf{U} = \mathbf{F}(\mathbf{U}), \tag{22}$$

where $\mathbf{U}$

### *2.3. Time integration*

For the time integration step, we employ the implicit Euler method. This technique consists in approximate the velocity and pressure fields in the subsequent time step $n+1$ by

$$\mathbf{U}_{n+1} = \mathbf{U}_n + \Delta t\dot{\mathbf{U}}_{n+1}. \tag{23}$$

Substituting this approximation in Eq. (22), the resulting nonlinear problem is given by

$$\left[\mathbf{M} + \Delta t\mathbf{K}\left(\mathbf{U}_{n+1}\right)\right]\mathbf{U}_{n+1} = \left[\mathbf{M} - \Delta t\mathbf{K}\left(\mathbf{U}_{n+1}\right)\right]\mathbf{U}_n + \Delta t\mathbf{F}\left(\mathbf{U}_{n+1}\right). \tag{24}$$

The nonlinear system obtained in Eq. (24) is solved by Newton iterations.

## 3. The Arlequin framework

The Arlequin framework is build on three main ideas [20, 10] (see Fig. 1):

- Superposing a discrete suitable local model ($\Omega_1$) to a subregion of a global one ($\Omega_0$) where the global discretization is unsuitable for representing the localized effects;
- Coupling the models in a sub-region of the overlapping zone ($\Omega_s$), called gluing zone ($\Omega_c$), and the definition of a convenient coupling operator;

- Assuring energy distribution between models by employing partition of unity weighting functions, ensuring the mechanical energy conservation.

Initially, let us assume the local model located in a particular zone of interest, where small-scale effects will occur, and with suitable discretization to capture such effects. The resulting computational domain $\Omega$ is then given by

$$\Omega = \Omega_0 \cup \Omega_1. \tag{25}$$

Similarly, the overlapping zone $\Omega_s$ is defined as

$$\Omega_s = \Omega_0 \cap \Omega_1, \tag{26}$$

$$\Omega_s = \Omega_c \cup \Omega_f, \tag{27}$$

$$\text{meas}(\Omega_c) > 0, \tag{28}$$

where $\Omega_f$ is called free zone.

For incompressible problems, even if both global and local models discretizations are stable according to the Ladyzhenskaya–Babuška–Brezzi (LBB) condition [24], the incompressibility constraint enforcement to both models can lead to a redundancy, resulting in a singular problem [19].

To overcome this issue, Jamond and Ben Dhia [19] proposes a methodology for imposing the incompressibility constraint at each point of the computational domain only once. Such methodology consists in choosing one model and eliminating the incompressibility constraint from its elements that are located partially or totally in the gluing zone. This simple alternative is possible because, as demonstrated by the authors, there is an incompressibility diffusion in partially incompressible finite elements, i.e., the displacement field in a finite element keeps divergence free even if the incompressibility constraint is applied only to a portion of it.

Thus, two choices are possible: removing the incompressibility constraint from the local or global model gluing zone, as shown in Figure 2. Notice that, in both cases the incompressibility constraint is completely removed from the global model free zone.

In this work, by employing PSPG stabilized finite elements for ~~circumventing~~ fulfilling the LBB condition, the use of equal order approximation functions for all problem variables is possible, and also, as both, local and global continuity equations are modified, incompressibility constraint can be kept for both models, eliminating the need for searching elements where incompressibility needs to be removed. Concerning the coupling operator, the choice of its space of functions can change significantly the solution, although both fine or coarse models approximation functions could be chosen [20]. When the coupling operator is defined in the local model, under some discretization conditions, the fine model solution is locked to the global one, while the opposite choice leads to a solution linked in an average sense [21]. However, it is more practical to define the coupling operator in the local model, especially in cases where local model moves over the global one, so that we develop this work over such assumption.

A standard definition of the coupling operator is given by

$$(\mathbf{w}, \boldsymbol{\lambda})_{\Omega_c} = \int_{\Omega_c} \kappa_0 \left[\mathbf{w} \cdot \boldsymbol{\lambda}\right] + \kappa_1 \left[\boldsymbol{\varepsilon}(\mathbf{w}) : \boldsymbol{\varepsilon}(\boldsymbol{\lambda})\right] \; d\Omega_c, \tag{29}$$

where $\boldsymbol{\lambda} = \{\lambda_x, \lambda_y\}$, is the Lagrange multiplier field. The constants $\kappa_0$ and $\kappa_1$ are strictly positive (see e.g. [10, 21] for more details). For $\kappa_0 > 0$ and $\kappa_1 = 0$ one obtain the so-called $L^2$ coupling operator. Otherwise, for $\kappa_0 > 0$ and $\kappa_1 > 0$ the $H^1$ coupling operator is obtained. Both options can be used, depending on the application and taking into account that the $L^2$ operator establishes, in a weak sense, the continuity of velocities ($\mathbf{u}_0 - \mathbf{u}_1 = \mathbf{0}$), while $H^1$ coupling operator ensures, also in a weak sense, the continuity of a linear combination of the velocities and its Laplacian ($\kappa_0 \left(\mathbf{u}_0 - \mathbf{u}_1\right) + \kappa_1 \nabla^2 \left(\mathbf{u}_0 - \mathbf{u}_1\right) = \mathbf{0}$) [21].

One can notice that, when applied to velocity, as in the Navier-Stokes finite element solution employed here, the Laplacian operator will introduce dissipation to the model, demanding a proper choice of $\kappa_0$ and $\kappa_1$. Thus, we assume $\kappa_0 = 1$ and $\kappa_1 = 0$, and propose a novel residual-based stabilization for the $L^2$ operator (see section 5.1.1) to ensure a better conditioning to the algebraic system.

Regarding energy distribution between models, a classical definition of partition of unity functions $\alpha_i$ is usually employed. More details on the definition of $\alpha_i$ is given in the next section.

## 4. The Residual-Based Arlequin formulation

Insert Proof of stability here and maybe change the last section.

## 5. Arlequin formulation for incompressible flows

In this section, for the sake of simplicity, we initially develop the residual-based Arlequin formulation for Stokes flow in 5.1, and later, in 5.2, we extend it to Navier-Stokes flows.

### *5.1. Stokes problem*

The incompressible Stokes flow governing equations are:

$$\nabla \cdot \boldsymbol{\sigma} + \rho \mathbf{f} = \mathbf{0}, \tag{30}$$

$$\nabla \cdot \mathbf{u} = 0. \tag{31}$$

As there is no convection, only PSPG stabilization is needed and the discrete stabilized monomodel problem can be written as

$$\left(\boldsymbol{\varepsilon}(\mathbf{w}^h), 2\mu\boldsymbol{\varepsilon}(\mathbf{u}^h)\right)_\Omega - \left(p^h, \nabla \cdot \mathbf{w}^h\right)_\Omega = \left(\mathbf{w}^h, \rho \mathbf{f}^h\right)_\Omega + \left(\mathbf{w}^h, \mathbf{h}^h\right)_{\Gamma_t}, \tag{32}$$

$$\left(q^h, \nabla \cdot \mathbf{u}^h\right)_\Omega + \left(\tau_{\mathrm{PSPG}} \frac{\nabla q^h}{\rho}, \mathbf{r}_{\mathrm{M}}\right)_\Omega = 0, \tag{33}$$

~~Let us adopt indexes 0 and 1 to represent respectively global and local models.~~ Analogously to the monomodel problem, the finite dimensional trial solution function spaces, $\mathcal{S}_{ui}^h$ and $\mathcal{S}_{pi}^h$, and the weighting function spaces by $\mathcal{V}_{ui}^h$ and $\mathcal{V}_{pi}^h$, are defined as

$$\mathrm{V}_{ui}^h = \left\{\mathbf{w}_i^h | \mathbf{w}_i^h(\cdot) \in H^{1h}(\Omega_i), \mathbf{w}_i^h = \mathbf{0} \text{ on } \Gamma_{Di}\right.$$
$$\mathcal{V}_{pi}^h = \mathcal{S}_{pi}^h.$$

The Lagrange multiplier trial and test spaces of functions are:

$$\mathcal{M}^h = \left\{\boldsymbol{\lambda}^h | \boldsymbol{\lambda}^h(\cdot) \in H^{1h}(\Omega_c)\right\} \tag{34}$$
$$\mathcal{Q}^h = \mathcal{M}^h. \tag{35}$$

For simplicity on writing the formulation, one consider only Dirichlet boundary conditions, so the Stokes problem in the Arlequin framework reads as: find $\left(\mathbf{u}_0^h, p_0^h, \mathbf{u}_1^h, p_1^h, \boldsymbol{\lambda}^h\right) \in \mathcal{S}_{u0}^h \times \mathcal{S}_{p0}^h \times \mathcal{S}_{u1}^h \times \mathcal{S}_{p1}^h \times \mathcal{M}^h$ such that $\forall \mathbf{w}_0^h \in \mathcal{V}_{u0}^h$, $\forall q_0^h \in \mathcal{V}_{p0}^h$, $\forall \mathbf{w}_1^h \in \mathcal{V}_{u1}^h$, $\forall q_1^h \in \mathcal{V}_{p1}^h$ and $\forall \boldsymbol{\zeta}^h \in \mathcal{Q}^h$,

$$\left(\boldsymbol{\varepsilon}(\mathbf{w}_0^h), 2\mu\alpha_0\boldsymbol{\varepsilon}(\mathbf{u}_0^h)\right)_{\Omega_0} - \left(\alpha_0 p_0^h, \nabla\cdot\mathbf{w}_0^h\right)_{\Omega_0} + \left(\boldsymbol{\lambda}^h, \mathbf{w}_0^h\right)_{\Omega_c} = \left(\mathbf{w}_0^h, \rho\alpha_0\mathbf{f}_0^h\right)_{\Omega_0}, \tag{36}$$
$$\left(q_0^h, \alpha_0\nabla\cdot\mathbf{u}_0^h\right)_{\Omega_0} + \left(\tau_{\mathrm{PSPG}}\frac{\nabla q_0^h}{\rho}, \mathbf{r}_{\mathrm{M}0}\right)_{\Omega_0} = 0, \tag{37}$$
$$\left(\boldsymbol{\varepsilon}(\mathbf{w}_1^h), 2\mu\alpha_1\boldsymbol{\varepsilon}(\mathbf{u}_1^h)\right)_{\Omega_1} - \left(\alpha_1 p_1^h, \nabla\cdot\mathbf{w}_1^h\right)_{\Omega_1} - \left(\boldsymbol{\lambda}^h, \mathbf{w}_1^h\right)_{\Omega_c} = \left(\mathbf{w}_1^h, \rho\alpha_1\mathbf{f}_1^h\right)_{\Omega_1}, \tag{38}$$
$$\left(q_1^h, \alpha_1\nabla\cdot\mathbf{u}_1^h\right)_{\Omega_1} + \left(\tau_{\mathrm{PSPG}}\frac{\nabla q_1^h}{\rho}, \mathbf{r}_{\mathrm{M}1}\right)_{\Omega_1} = 0, \tag{39}$$
$$\left(\boldsymbol{\zeta}^h, \mathbf{u}_0^h - \mathbf{u}_1^h\right)_{\Omega_c} = 0, \tag{40}$$

where the coupling operator $l(\cdot,\cdot)$ follows the definition of Eq. (29), with $\kappa_0 = 1$ and $\kappa_1 = 0$. The bilinear forms are given by:

$$a_i\left(\mathbf{w}_i^h, \mathbf{u}_i^h\right) = \int_{\Omega_i} \alpha_i 2\mu\boldsymbol{\varepsilon}(\mathbf{w}_i^h) : \boldsymbol{\varepsilon}(\mathbf{u}_i^h)\, d\Omega_i, \tag{41}$$
$$b_i\left(q_i^h, \mathbf{u}_i^h\right) = \int_{\Omega_i} \alpha_i\ q_i^h \nabla\cdot\mathbf{u}_i^h\ d\Omega_i, \tag{42}$$
$$b_i\left(p_i^h, \mathbf{w}_i^h\right) = -\int_{\Omega_i} \alpha_i\ p_i^h \nabla\cdot\mathbf{w}_i^h\ d\Omega_i, \tag{43}$$
$$d_i\left(q_i^h, \mathbf{r}_{\mathrm{M}i}\right) = \sum_{e=1}^{n_{\mathrm{el}}} \int_{\Omega^e} \frac{\tau_{\mathrm{PSPG}}}{\rho} \nabla q_i^h \cdot \mathbf{r}_{\mathrm{M}i}\left(\mathbf{u}_i^h, p_i^h, \boldsymbol{\lambda}^h\right)\ d\Omega_i, \tag{44}$$

and

$$f_i\left(\mathbf{w}_i^h\right) = \int_{\Omega_i} \alpha_i \rho\ \mathbf{w}_i^h \cdot \mathbf{f}_i^h\ d\Omega_i + \int_{\Gamma_{ti}} \alpha_i\ \mathbf{w}_i^h \cdot \mathbf{h}_i^h\ d\Gamma_i, \tag{45}$$

where the energy weight functions $\alpha_i$ are given by

$$\begin{cases} \alpha_i \in [0,1] & \text{in } \Omega, \\ \alpha_0 + \alpha_1 = 1 & \text{in } \Omega, \\ \alpha_i = 1 & \text{in } \Omega_i \setminus \Omega_j,\ i \neq j, \\ \alpha_i = c_i > 0 & \text{in } \Omega_f, \end{cases} \tag{46}$$

where $c_i$ is a constant arbitrarily small to the Arlequin method be relevant [10]. Finally, the residual of momentum equation ($\mathbf{r}_{\mathrm{M}i}$) is written as:

$$\mathbf{r}_{\mathrm{M}i}\left(\mathbf{u}_i^h, p_i^h, \boldsymbol{\lambda}^h\right) = \alpha_i \rho \mathbf{f}_i^h + \alpha_i \nabla \cdot \boldsymbol{\sigma}\left(\mathbf{u}_i^h, p_i^h\right) + \chi(i)\boldsymbol{\lambda}^h, \tag{47}$$

with

$$\chi(i) = \begin{cases} (-1)^i & \text{if } \mathbf{x} \in \Omega_c, \\ 0 & \text{if } \mathbf{x} \notin \Omega_c. \end{cases} \tag{48}$$

As one can see, one possible interpretation of the problem defined by (36)-(40) is that it is equivalent to gluing two domains with different thicknesses with magnitude equal to the energy weight function $\alpha_i$, considering velocity and pressure fields constants on thickness direction. The PSPG stabilization provides pressure-dependent additional terms to the continuity equation, which overcomes the redundancy problems on stable finite elements [19], allowing hydrostatic stress (pressure) energy can also be weighted by $\alpha_0$ and $\alpha_1$.

### *5.1.1. Residual-Based Stabilized Arlequin Formulation*

One drawback of the Arlequin framework consists on the difficulty of constructing a well-conditioned algebraic system of equations. As demonstrated by Ben Dhia [29], though the simplicity of $L^2$ operator by the weak enforcement of $\mathbf{u}_0 = \mathbf{u}_1$ through the gluing zone, unless properly scaled it can lead to an ill conditioned associated discrete Arlequin problem. On the other side, a better-conditioned problem is obtained when applying $H^1$ coupling operator. However, it enforces a linear combination of velocities and its Laplacian, which is not always desirable. In addition, the choice of parameters $\kappa_0$ and $\kappa_1$ is not trivial.

To overcome the drawbacks of the $L^2$ coupling operator, we propose to add to the coupling equation, the following stabilizing term:

$$e\left(\boldsymbol{\zeta}^h, \mathbf{r}_{\mathrm{M}i}\right) = \sum_{i=0}^{n_{dom}} \sum_{e=1}^{n_{\mathrm{el}}} \int_{\Omega_c^e} \chi(i) \frac{\tau_{ARLQ}}{\rho} \nabla \boldsymbol{\zeta}^h : \nabla \mathbf{r}_{\mathrm{M}i}\left(\mathbf{u}_i^h, p_i, {}^h \boldsymbol{\lambda}^h\right)\ d\Omega_{ci} \tag{49}$$

where $n_{dom}$ is the number of sub-domains and $\tau_{ARLQ}$ is the stabilization parameter.

The parameter $\tau_{ARLQ}$ is calculated as an element-vector-based stabilization parameter. Element-vector-based stabilization parameters were introduced and tested in [30] and also tested in [27], and described in [28]. Here it is given as

$$\tau_{ARLQ} = \frac{\|\mathbf{n}\|}{\|\mathbf{k}_i\|} \tag{50}$$

where $\mathbf{n}$ and $\mathbf{k}_i$ are element-level vectors defined as

$$\mathbf{n} = \int_{\Omega^e} \boldsymbol{\zeta}^h \cdot \left(\mathbf{u}_0^h - \mathbf{u}_1^h\right) d\Omega_c, \tag{51}$$

$$\mathbf{k}_i = \int_{\Omega^e} \nabla^2 \boldsymbol{\zeta}^h : 2\mu \nabla \cdot \boldsymbol{\varepsilon}\left(\mathbf{u}_i^h\right) d\Omega_c. \tag{52}$$

Thus, the Residual-based stabilized Arlequin formulation for Stokes flows is written as

$$\left(\boldsymbol{\varepsilon}(\mathbf{w}_0^h), 2\mu\alpha_0\boldsymbol{\varepsilon}(\mathbf{u}_0^h)\right)_{\Omega_0} - \left(\alpha_0 p_0^h, \nabla\cdot\mathbf{w}_0^h\right)_{\Omega_0} + \left(\boldsymbol{\lambda}^h, \mathbf{w}_0^h\right)_{\Omega_c} = \left(\mathbf{w}_0^h, \rho\alpha_0\mathbf{f}_0^h\right)_{\Omega_0}, \tag{53}$$

$$\left(q_0^h, \alpha_0\nabla\cdot\mathbf{u}_0^h\right)_{\Omega_0} + \left(\tau_{\mathrm{PSPG}}\frac{\nabla q_0^h}{\rho}, \mathbf{r}_{\mathrm{M0}}\right)_{\Omega_0} = 0, \tag{54}$$

$$\left(\boldsymbol{\varepsilon}(\mathbf{w}_1^h), 2\mu\alpha_1\boldsymbol{\varepsilon}(\mathbf{u}_1^h)\right)_{\Omega_1} - \left(\alpha_1 p_1^h, \nabla\cdot\mathbf{w}_1^h\right)_{\Omega_1} - \left(\boldsymbol{\lambda}^h, \mathbf{w}_1^h\right)_{\Omega_c} = \left(\mathbf{w}_1^h, \rho\alpha_1\mathbf{f}_1^h\right)_{\Omega_1}, \tag{55}$$

$$\left(q_1^h, \alpha_1\nabla\cdot\mathbf{u}_1^h\right)_{\Omega_1} + \left(\tau_{\mathrm{PSPG}}\frac{\nabla q_1^h}{\rho}, \mathbf{r}_{\mathrm{M1}}\right)_{\Omega_1} = 0, \tag{56}$$

$$\left(\boldsymbol{\zeta}^h, \mathbf{u}_0^h - \mathbf{u}_1^h\right)_{\Omega_c} + \left(\frac{\tau_{ARLQ}}{\rho}\nabla\boldsymbol{\zeta}^h, \nabla\mathbf{r}_{\mathrm{M0}} - \nabla\mathbf{r}_{\mathrm{M1}}\right)_{\Omega_c} = 0, \tag{57}$$

In a matrix notation, the problem can be written as

$$\begin{bmatrix} \mathbf{K}_0 & \mathbf{0} & \widehat{\mathbf{L}}_0 \\ \mathbf{0} & \mathbf{K}_1 & -\widehat{\mathbf{L}}_1 \\ \mathbf{L}_0^T & -\mathbf{L}_1^T & \mathbf{E} \end{bmatrix} \begin{Bmatrix} \mathbf{U}_0 \\ \mathbf{U}_1 \\ \boldsymbol{\Lambda} \end{Bmatrix} = \begin{Bmatrix} \mathbf{F}_0 \\ \mathbf{F}_1 \\ \mathbf{0} \end{Bmatrix}. \tag{58}$$

REVISAR! Notice that on the residual-based Arlequin stabilization, differently from the $H^1$ coupling operator, new terms are introduced on the global matrix diagonal.

Notice that, differently from the $H^1$ coupling operator, the residual-based Arlequin stabilization improves stability by adding new terms to the global matrix diagonal.

*5.1.2. Numerical test - pressurized fluid in a holed chamber*

In order to verify the proposed formulation for Stokes flows, we simulate a problem presented by Jamond and Ben Dhia [19], which consists of a chamber filled by a viscous fluid, according to Fig. 3. As boundary conditions, we assume free slip walls and free-stream traction at the chamber hole. At left boundary (piston location), a uniform horizontal velocity profile with unit magnitude is applied. The

fluid dynamic viscosity and density are $\mu = 1/3$ and $\rho = 1.0$, respectively for the entire domain. All simulations are performed with quadratic triangular finite elements with equal order approximation for velocity, pressure and Lagrange multiplier fields. Linear continuous energy weight functions are employed and the results are compared to Jamond and Ben Dhia [19] and to a monomodel simulation.

The aim of this example is to compare the Residual-Based Stabilized Arlequin formulation results to those presented by Jamond and Ben Dhia [19], using P2P1 Taylor-Hood finite elements. In order to do so, we perform 3 different simulations for each considered case:

*i* Only pressure stabilization is considered and $L^2$ coupling operator is employed ($\kappa_0 = 1$ and $\kappa_1 = 0$);

*ii* Only pressure stabilization is considered and $H^1$ coupling operator is employed with constants $\kappa_0 = 4$ and $\kappa_1 = 1$;

*iii* Pressure and Lagrange multipliers stabilizations are considered and $L^2$ coupling operator is employed ($\kappa_0 = 1$ and $\kappa_1 = 0$).

It is also important to mention, that the reference considers constant discontinuous energy weight functions $\alpha_i$. Two different local domain sizes are considered for the initial analysis. The first local domain (Fig. 4a) is wider, keeping the gluing zone $\Omega_c$ farther from the hole, while the second one (Fig. 4b) places the gluing zone over the hole limits. A monomodel discretization (128x64 finite elements) is also considered for reference. The adopted meshes and their respectively gluing zones are illustrated in Fig. 4.

To compare quantitatively the results to the reference, we use the error on the global flow mass conservation, computed as the relation between the chamber output and input mass flows ($Q$ and $Q_{inp}$), given by

$$\varepsilon_Q = 100\frac{Q - Q_{inp}}{Q_{inp}}. \tag{59}$$

We found $\varepsilon_Q = -12.88$ for mesh 1 and $\varepsilon_Q = -18.83$ for mesh 2. Comparing to the reference, among the mesh configurations tested by Jamond and Ben Dhia [19], the best result for $\varepsilon_Q$ presented for triangular finite elements is equal to $\varepsilon_Q = -16.25$ for mesh 1 configuration. For mesh 2, in most of the cases tested by Jamond and Ben Dhia [19], a locking phenomenon is observed when there are no coarse model elements completely included on the free zone ($\Omega_f$).

Following, we perform a convergence analysis regarding $\varepsilon_Q$. by considering structured meshes with characteristic lengths $h$ of 1/2, 1/4 and 1/8. The fine model geometry was set as the same of mesh 1 in figure 4.

For the global model, two scenarios are considered: 1) keeping it with the coarsest discretization ($h$=1/2) and 2) varying the characteristic length of the fine model; and making the same discretization level for both meshes. Both scenarios were tested for $H^1$ coupling operator, with $\kappa_0$ and $\kappa_1$ the same as in case A and the stabilized $L^2$ operator. The same convergence analysis considering a monomodel discretization is taken as reference. The results obtained for both cases are presented in Fig. 5.

As expected, when the coarse model discretization is kept constant and just the fine model is refined, bigger values of $\varepsilon_Q$ are obtained. It is due to a bigger influence of the coarse model discretization error in the global solution for this particular problem.

For the case of $h$=1/8 the Lagrange multiplier components over the line $y = 2$ in the first layer (left) of the gluing zone is presented in Fig. 6. One can notice that an oscillatory Lagrange multiplier field is obtained when employing the $L^2$ coupling operator due to the linear algebraic system ill conditioning. Both $H^1$ and stabilized $L^2$ coupling operators gives continuous and smooth Lagrange multiplier fields. It is also important to notice that in the $L^2$ coupling, the Lagrange multiplier field represent only the coupling force field, while in the $H^1$ it has also the effect of coupling stresses included. Lagrange multipliers fields for the $L^2$ and stabilized $L^2$ coupling operators are presented in Fig. 7.

The results show that the proposed formulation can be more precise and confirms it to be locking-free without the need for removing incompressibility constraint, one overcoming problems observed on Taylor-Hood finite elements. The oscillatory behavior in the Lagrange multiplier field, observed when $L^2$ coupling operator is employed, can easily lead to convergence loss and instability in transient analysis. However, the proposed stabilization revealed to be very efficient to suppress such oscillations without compromising mass conservation convergence, as one can see from Fig. 6.

### *5.2. Extension to Navier-Stokes flows*

The Arlequin problem for the complete incompressible Navier-Stokes equations can be obtained by adding the convective and time-dependent terms to the Stokes problem developed on the previous section, weighted by the respective model energy weight function ($\alpha_i$).

At this point, SUPG and LSIC stabilizations are also introduced and the resulting Arlequin problem writes: find $\left(\mathbf{u}_0^h, p_0^h, \mathbf{u}_1^h, p_1^h, \boldsymbol{\lambda}^h\right) \in \mathcal{S}_{u0}^h \times \mathcal{S}_{p0}^h \times \mathcal{S}_{u1}^h \times \mathcal{S}_{p1}^h \times \mathcal{M}^h$ such that $\forall \mathbf{w}_0^h \in \mathcal{V}_{u0}^h$, $\forall q_0^h \in \mathcal{V}_{p0}^h$, $\forall \mathbf{w}_1^h \in \mathcal{V}_{u1}^h$, $\forall q_1^h \in \mathcal{V}_{p1}^h$ and $\forall \boldsymbol{\zeta}^h \in \mathcal{Q}^h$

$$\begin{aligned}\left(\mathbf{w}_0^h, \rho\alpha_0 \frac{\partial \mathbf{u}_0^h}{\partial t}\right)_{\Omega_0} + \left(\boldsymbol{\varepsilon}(\mathbf{w}_0^h), 2\mu\alpha_0\boldsymbol{\varepsilon}(\mathbf{u}_0^h)\right)_{\Omega_0} + \left(\rho\alpha_0\mathbf{u}_0^h; \mathbf{w}_0^h, \nabla\mathbf{u}_0^h\right)_{\Omega_0} - \left(\alpha_0 p_0^h, \nabla\cdot\mathbf{w}_0^h\right)_{\Omega_0} \\ + \left(\tau_{\mathrm{SUPG}}\mathbf{u}_0^h\cdot\nabla\mathbf{w}_0^h, \mathbf{r}_{\mathrm{M0}}\right)_{\Omega_0} + \left(\nu_{\mathrm{LSIC}}\nabla\cdot\mathbf{w}_0^h, \mathbf{r}_{\mathrm{C0}}\right)_{\Omega_0} + \left(\boldsymbol{\lambda}^h, \mathbf{w}_0^h\right)_{\Omega_c} = \left(\mathbf{w}_0^h, \rho\alpha_0\mathbf{f}_0^h\right)_{\Omega_0},\end{aligned} \tag{60}$$

$$\left(q_0^h, \alpha_0\nabla\cdot\mathbf{u}_0^h\right)_{\Omega_0} + \left(\tau_{\mathrm{PSPG}}\frac{\nabla q_0^h}{\rho}, \mathbf{r}_{\mathrm{M0}}\right)_{\Omega_0} = 0, \tag{61}$$

$$\begin{aligned}\left(\mathbf{w}_1^h, \rho\alpha_1 \frac{\partial \mathbf{u}_1^h}{\partial t}\right)_{\Omega_1} + \left(\boldsymbol{\varepsilon}(\mathbf{w}_1^h), 2\mu\alpha_1\boldsymbol{\varepsilon}(\mathbf{u}_1^h)\right)_{\Omega_1} + \left(\rho\alpha_1\mathbf{u}_1^h; \mathbf{w}_1^h, \nabla\mathbf{u}_1^h\right)_{\Omega_1} - \left(\alpha_1 p_1^h, \nabla\cdot\mathbf{w}_1^h\right)_{\Omega_1} \\ + \left(\tau_{\mathrm{SUPG}}\mathbf{u}_1^h\cdot\nabla\mathbf{w}_1^h, \mathbf{r}_{\mathrm{M1}}\right)_{\Omega_1} + \left(\nu_{\mathrm{LSIC}}\nabla\cdot\mathbf{w}_1^h, \mathbf{r}_{\mathrm{C1}}\right)_{\Omega_1} - \left(\boldsymbol{\lambda}^h, \mathbf{w}_1^h\right)_{\Omega_c} = \left(\mathbf{w}_1^h, \rho\alpha_1\mathbf{f}_1^h\right)_{\Omega_1},\end{aligned} \tag{62}$$

$$\left(q_1^h, \alpha_1\nabla\cdot\mathbf{u}_1^h\right)_{\Omega_1} + \left(\tau_{\mathrm{PSPG}}\frac{\nabla q_1^h}{\rho}, \mathbf{r}_{\mathrm{M1}}\right)_{\Omega_1} = 0, \tag{63}$$

$$\left(\boldsymbol{\zeta}^h, \mathbf{u}_0^h - \mathbf{u}_1^h\right)_{\Omega_c} + \left(\frac{\tau_{ARLQ}}{\rho}\nabla\boldsymbol{\zeta}^h, \nabla\mathbf{r}_{\mathrm{M0}} - \nabla\mathbf{r}_{\mathrm{M1}}\right)_{\Omega_c} = 0, \tag{64}$$

The residuals are now defined as

$$r_{\mathrm{C}i}\left(\mathbf{u}_i^h\right) = \alpha_i\nabla\cdot\mathbf{u}_i^h \tag{65}$$

and

$$\mathbf{r}_{\mathrm{M}i}\left(\mathbf{u}_i^h, p_i^h, \boldsymbol{\lambda}^h\right) = \alpha_i \rho \left(\frac{\partial \mathbf{u}_i^h}{\partial t} + \mathbf{u}_i^h \cdot \nabla \mathbf{u}_i^h - \mathbf{f}_i^h\right) - \alpha_i \nabla \cdot \boldsymbol{\sigma}\left(\mathbf{u}_i^h, p_i^h\right) + \chi(i)\boldsymbol{\lambda}^h. \tag{66}$$

The stabilization parameters $\tau_{\mathrm{SUPG}i}$, $\tau_{\mathrm{PSPG}i}$ and $\nu_{\mathrm{LSIC}i}$ are the same from [26] and [28],calculated from equations (12)-(13) considering model $i$ values. The coupling operator stabilization parameter $\tau_{ARLQ}$ is constant by local model element and are calculated as element-vector-based stabilization parameters as introduced in [30], according to:

$$\tau_{ARLQ} = \left(\frac{1}{\tau_{A1}^2} + \frac{1}{\tau_{A2}^2} + \frac{1}{\tau_{A3}^2}\right)^{-\frac{1}{2}} \tag{67}$$

where

$$\tau_{A1} = \frac{\|\mathbf{n}\|}{\|\mathbf{t}_i\|}, \tag{68}$$

$$\tau_{A2} = \frac{\|\mathbf{n}\|}{\|\mathbf{j}_i\|}, \tag{69}$$

$$\tau_{A3} = \frac{\|\mathbf{n}\|}{\|\mathbf{k}_i\|}, \tag{70}$$

with $\mathbf{n}$ and $\mathbf{k}_i$ given by Eq. (51) and (52). Similarly, $\mathbf{t}_i$ and $\mathbf{j}_i$ are given by

$$\mathbf{t}_i = \int_{\Omega^e} \nabla \boldsymbol{\zeta}^h : \nabla\left(\mathbf{u}_i^h \cdot \nabla \mathbf{u}_i^h\right) d\Omega_c, \tag{71}$$

$$\mathbf{j}_i = \int_{\Omega^e} \nabla \boldsymbol{\zeta}^h : \nabla\left(\frac{\partial \mathbf{u}_i^h}{\partial t}\right) d\Omega_c. \tag{72}$$

Applying the generalized trapezoidal time-marching procedure (Section 2.3) to (60)-(64), and writing using matrix notation, the resulting nonlinear system to be solved is given by

$$\begin{bmatrix} \mathbf{M}_0 & \mathbf{0} & \mathbf{0} \\ \mathbf{0} & \mathbf{M}_1 & \mathbf{0} \\ \mathbf{A}_0 & \mathbf{A_1} & \mathbf{0} \end{bmatrix} \begin{Bmatrix} \dot{\mathbf{U}}_0 \\ \dot{\mathbf{U}}_1 \\ \dot{\boldsymbol{\Lambda}} \end{Bmatrix} + \begin{bmatrix} \mathbf{K}_0\left(\mathbf{U}_0\right) & \mathbf{0} & \widehat{\mathbf{L}}_0 \\ \mathbf{0} & \mathbf{K}_1\left(\mathbf{U}_1\right) & -\widehat{\mathbf{L}}_1 \\ \mathbf{L}_0^T & -\mathbf{L}_1^T & \mathbf{E} \end{bmatrix} \begin{Bmatrix} \mathbf{U}_0 \\ \mathbf{U}_1 \\ \boldsymbol{\Lambda} \end{Bmatrix} = \begin{Bmatrix} \mathbf{F}_0 \\ \mathbf{F}_1 \\ \mathbf{0} \end{Bmatrix}. \tag{73}$$

## 6. Numerical examples

In this section, we present the numerical simulation of a set of benchmark problems. The same triangular finite elements with quadratic basis functions presented in section 5.1.2 are employed, with linear continuous energy weight functions.

### *6.0.1. Flow over a flat plate*

In this example, we aim to experiment the multiscale robustness of the method by simulating a high Reynods number problem. A flat plate of dimension equal to the unity located at a distance of 0.5 from

the inflow boundary is subjected to a parallel flow at Re = $10^6$, taking as reference inlet velocity $u_\infty$ and the plate length. The computational domain, as well as boundary conditions are presented in Fig. 8.

Unfitted local/global unstructured finite element discretizations are employed. The fine model is 0.15 height and covers the entire plate surface with 823 elements and 1728 nodes. The first finite element layer has a thickness of $1.10^{-4}$, in agreement with the numerical tests performed in [31]. A 0.05 thick layer with 108 finite elements and 273 nodes composes the gluing zone. For the global model, a coarse discretization with 363 elements and 778 nodes is used, as illustrated in Fig. 9.

The solution is obtained by a steady analysis and in Fig. 10, one compare the numerically obtained local skin friction coefficient $C_f$ along the plate surface, defined as

$$C_f = \frac{2\nu}{u_\infty^2} \left. \frac{\partial u_x}{\partial y} \right|_{wall}, \tag{74}$$

to the Blasius solution, obtained by the classical boundary layer theory (details are found in [32]), given by

$$C_f^{Blasius} = \frac{0.664}{\sqrt{u_\infty d/\nu}}, \tag{75}$$

where $d$ is the distance from the leading edge of the plate.

One can see from Fig. 10 that the proposed formulation produced results nearly coincident to the theoretical ones. Figure 11 shows the pressure distribution, where one can observe continuity and smoothness in the local/global domains transition.

*6.0.2. Lid-driven cavity flow*

The lid-driven square cavity flow is one of the most popular benchmark problems for the verification of incompressible flow solvers. It consists of a square cavity filled with fluid and bounded by three rigid walls with no-slip conditions and an upper moving lid with horizontal unit velocity, as detailed in Fig. 12.

In order to get a reference solutions, a monomodel discretization is employed with $h$=1/20, 800 elements and 1681 nodes. For the Arlequin simulation, we take the monomodel mesh as global discretization and overlap a 0.4 thick finer model discretization close to the cavity boundaries, and with $h$=1/40, 2048 elements and 4352 nodes. The gluing zone is 0.2 thick, as illustrated in Fig. 13.

For all cases, transient simulations are carried out until the velocity field is considered to be steady, i.e., $\|\mathbf{u}_t^h - \mathbf{u}_{t-1}^h\|/\|\mathbf{u}_t^h\| < 10^{-6}$.

Flows with three different Reynolds are simulated (Re = 1000, 5000 and 10000), taking the cavity edge as characteristic length. Results obtained for all considered cases in comparison with those presented by Ghia et al. [33] are shown in Fig. 14.

As one can see, both monomodel and Arlequin model adopted discretizations can represent properly the flow behavior for low Reynolds numbers. However, when Re is increased, the adopted monomodel discretization cannot capture the fine scales phenomena, mostly close to the cavity edges.

The Arlequin model steady-state solutions for velocity and pressure fields are shown in Figs. 15 and 16.

*6.0.3. Flow over a circular cylinder*

In order to test the formulation for time dependent problems, we simulate the classical problem of flow over a circular cylinder. The computational domain consists in a circular cylinder with unit diameter, centered in the coordinate system origin. The inflow boundary is located 18 units upstream from the cylinder. Upper and lower boundaries are 25 units away from the cylinder. Top and bottom boundaries are slip wall type (zero normal direction and free tangential velocities). The outflow boundary is located 38 units downstream from the cylinder and has traction free boundary condition.

Global model is discretized by 4486 elements and 9073 nodes. The local model is designed with two concentric circles with radius 0.5 and 3.0, where the inner corresponds to the cylinder no slip wall. For the local model, we adopt a mesh with 5648 quadratic triangular elements and 11500 nodes. The coupling zone has unit thickness, 1260 elements and 2696 nodes, as shown in Fig. 17.

Three different Reynolds number flows are considered: Re = 20, 100 and 200. The adopted time step is $\Delta t = 0.05$. During the analysis, separation angle $\theta_s$, defined as the point of zero friction, is monitored and compared to the expression proposed by Wu et al. [34]:

$$\theta_s = 95.88 + 264.76\ \mathrm{Re}^{-1/2} - 619.01\ \mathrm{Re}^{-1} + 1042.4\ \mathrm{Re}^{-3/2}. \tag{76}$$

For the Re = 20, a symmetric steady flow is obtained. However, for Re = 100 and Re = 200, a laminar von Kármán vortex shedding is observed, obviously resulting a time-dependent separation angle so that the time-averaged value is used for comparison. Fig. 18 plots the separation angle vs. Re numerically obtained and compares to the reference equation.

As one can observe, the numerical results are in good agreement with the reference values, confirming the robustness of the technique. In Fig. 19, the streamlines for the separation angle time-averaged value are presented, illustrating the flow pattern variation according to the Reynolds number.

For Re = 20, we get a drag coefficient $C_D = 2.075$. For the other cases, maximum lift and average drag coefficient ($C_D$ and $C_L$) are presented in Table 1, while the time history is show in Fig. 20. The obtained values are in agreement with references as can be verified in Table 1.

Table 1: Flow over a circular cylinder: drag and lift coefficients

| | Re=100 | | | Re=200 | | |
|---|---|---|---|---|---|---|
| | $C_{L,max}$ | $C_{D,ave}$ | St | $C_{L,max}$ | $C_{D,ave}$ | St |
| Present study | 0.272 | 1.31 | 0.160 | 0.622 | 1.30 | 0.189 |
| Ding et al. [35] | 0.28 | 1.33 | 0.164 | 0.60 | 1.33 | 0.196 |
| Liu et al. [36] | 0.339 | 1.35 | 0.164 | 0.69 | 1.31 | 0.192 |
| Qu et al. [37] | 0.222 | 1.32 | 0.165 | 0.468 | 1.32 | 0.196 |
| Weymouth and Yue [38] | 0.33 | 1.35 | 0.167 | 0.69 | 1.34 | 0.195 |

Finally, velocity and pressure fields for time averaged separation angle are plotted on Fig. 21 and 22, respectively.

#### *6.0.4. Flow past a stationary NACA 0012*

In this example, we study the flow over a NACA 0012 airfoil with an angle of attack of 10°. The leading edge of the airfoil is located at the origin and the inflow boundary is 6 chord lengths upstream to the airfoil. Slip wall conditions are applied to upper and lower boundaries, both located $6cl$ (6 times the airfoil chord length) far from the airfoil and zero traction is applied to the outflow boundary. The considered Reynolds number is Re = 1000, computed with basis on the airfoil chord and the inflow velocity.

We adopt a mesh with 8413 quadratic triangular elements and 11949 nodes for the global model. The fine model is bounded by a curvilinear mesh of about $0.5cl$ far from the airfoil and discretized by 5836 quadratic triangular elements and 11949 nodes. The gluing zone is defined with a thickness of $0.2cl$, containing 592 elements and 1336 nodes, as shown in Fig. 23. The employed time step for all analysis is $\Delta t = 0.01$.

The simulations are performed considering $L^2$ coupling operator without stabilization and stabilized $L^2$ coupling operator. A monomodel with 10978 elements, 22282 nodes and same refinement level close to the airfoil is taken as reference.

Vortex shedding is observed on the flow for the Reynolds number chosen, resulting the lift and drag coefficients presented in Fig. 24. Time averaged values of $C_{D,ave} = 0.164$ and $C_{L,ave} = 0.41$ were obtained ~~no~~ on both $L^2$ and stabilized $L^2$ simulations and are in agreement to the values presented by Tezduyar et al. [39]: about 0.165 and 0.425, respectively.

Taking T as a lift coefficient period, the snapshots of a complete cycle steady stabilized-$L^2$ solution for velocity and pressure fields is presented on Fig. 25 and 26, respectively.

## 7. Conclusions

In this work, we explore the Arlequin method for the simulation of incompressible flows, introducing the Arlequin framework to the CFD context, and showing it as a robust and precise tool for considering local effects in complex nonlinear flows, as one can confirm from the proposed numerical tests.

In order to keep the multiscale method more suitable for incompressible Navier-Stokes problems, we propose a novel residual-based stabilized Arlequin formulation, which improves the conditioning of the resulting algebraic system, without changing the compatibility equation of the Lagrange multiplier-based problem. The results obtained with the proposed stabilization is compared to the other two coupling operators vastly employed on previous works ($L^2$ and $H^1$) by several numerical examples. According to the results obtained, the technique shown to be suitable for the simulation of incompressible flow problems even for very high Reynolds numbers and keeping the coupling Lagrange multipliers as a stable force field gluing local and global models.

The use of LBB-stabilized finite elements, also allows reducing the preprocessing step operations since there is no concern about removing the incompressibility constrain from certain elements as in previous Arlequin formulation applied to incompressible medias, also simplifying computational implementation.

The formulation robustness is demonstrated by many different tests with coincident overlapped finite element models, completely unstructured/non-coincident ones, Stokes problem, convection dominated Navier-Stokes steady and transient problems. This allow us to consider this formulation to be applied, in future works, to moving boundary problems, where localized effects, like boundary layers, are close to the moving boundary, so that only the local mesh needs to be dynamically deformed to accommodate boundary movements. Among such problems, one can consider large displacement fluid-structure interaction.

## Acknowledgments

This study was financed in part by the Coordenação de Aperfeiçoamento de Pessoal de Nível Superior - Brasil (CAPES) - Finance Code 001. The authors are also thankful to the, Brazilian National Council for Research and Technological Development (CNPq), grants 141015/2016-0 and 310482/2016-0, and the São Paulo Research Foundation (FAPESP), grant #2016/25520-5, for the financial support.

## References

[1] T. J. R. Hughes, Multiscale phenomena: Green's functions, the Dirichlet-to-Neumann formulation, subgrid scale methods, bubbles and the origins of stabilized methods, Comput. Methods Appl. Mech. Engrg 127 (1995) 387–401.

[2] J. M. Melenk, I. Babuska, The partition of unity finite element method: Basic theory and applications, Computer Methods in Applied Mechanics and Engineering 139 (1) (1996) 289–314.

[3] T. Strouboulis, K. Copps, I. Babuska, The generalized finite element method, Computer Methods in Applied Mechanics and Engineering 190 (32–33) (2001) 4081–4193.

[4] T. Belytschko, T. Black, Elastic crack growth in finite elements with minimal remeshing, International Journal for Numerical Methods in Engineering 45 (5) (1999) 601–620.

[5] J. Fish, The s-version of the finite element method, Computers & Structures 43 (3) (1992) 539–547.

[6] J. Fish, V. Belsky, Multi-grid method for periodic heterogeneous media Part 2: Multiscale modeling and quality control in multidimensional case, Computer Methods in Applied Mechanics and Engineering 126 (1) (1995) 17–38.

[7] J. L. Steger, J. A. Benek, On the use of composite grid schemes in computational aerodynamics, Computer Methods in Applied Mechanics and Engineering 64 (1–3) (1987) 301–320, ISSN 0045-7825.

[8] F. Brezzi, J.-L. Lions, O. Pironneau, Analysis of a Chimera method, Comptes Rendus de l'Académie des Sciences - Series I - Mathematics 332 (7) (2001) 655 – 660.

[9] H. Ben Dhia, Multiscale mechanical problems: The Arlequin method, Comptes Rendus Acad. Sci. Sér. Ilb. 326 (1998) 899–904.

[10] H. Ben Dhia, Further insights by Theoretical Investigations of the Multiscale Arlequin Method, International Journal for Multiscale Computational Engineering 6 (3) (2008) 215–232.

[11] H. Ben Dhia, O. Jamond, On the use of XFEM within the Arlequin framework for the simulation of crack propagation, Computer Methods in Applied Mechanics and Engineering 199 (21-22) (2010) 1403–1414.

[12] H. Ben Dhia, C. Zammali, Level-sets fields, placement and velocity based formulations of contact-impact problems, International Journal for Numerical Methods in Engineering 69 (2007) 2711–2735.

[13] H. Ben Dhia, M. Torkhani, Modeling and computation of fretting wear of structures under sharp contact, International Journal for Numerical Methods in Engineering 85 (2011) 61–83.

[14] S. Prudhomme, L. Chamoin, H. Ben Dhia, P. T. Bauman, An adaptive strategy for the control of modeling error in two-dimensional atomic-to-continuum coupling simulations, Computer Methods in Applied Mechanics and Engineering 198 (21) (2009) 1887–1901, advances in Simulation-Based Engineering Sciences – Honoring J. Tinsley Oden.

[15] L. Chamoin, S. Prudhomme, H. Ben Dhia, T. Oden, Ghost forces and spurious effects in atomic-to-continuum coupling methods by the Arlequin approach, International Journal for Numerical Methods in Engineering 83 (8-9) (2010) 1081–1113.

[16] R. Cottereau, D. Clouteau, H. Ben Dhia, C. Zaccardi, A stochastic-deterministic coupling method for continuum mechanics, Computer Methods in Applied Mechanics and Engineering 200 (47) (2011) 3280 – 3288, ISSN 0045-7825.

[17] S. M. Nazeer, F. Bordeu, A. Leygue, F. Chinesta, Arlequin based PGD domain decomposition, Computational Mechanics 54 (5) (2014) 1175–1190, ISSN 1432-0924.

[18] D. Néron, H. Ben Dhia, R. Cottereau, A decoupled strategy to solve reduced-order multimodel problems in the PGD and Arlequin frameworks, Computational Mechanics 57 (4) (2016) 509–521, ISSN 1432-0924.

[19] O. Jamond, H. Ben Dhia, Incompressibility in the multimodel Arlequin framework, Int. J. Numer. Meth. Engng. 94 (2013) 374–399.

[20] H. Ben Dhia, G. Rateau, The Arlequin method as a flexible engineering design tool, International Journal for Numerical Methods in Engineering 62 (11) (2005) 1442–1462.

[21] P.-A. Guidault, T. Belytschko, On the L2 and the H1 couplings for an overlapping domain decomposition method using Lagrange multipliers, International Journal for Numerical Methods in Engineering 70 (3) (2007) 322–350, ISSN 1097-0207.

[22] T. Tezduyar, Stabilized Finite Element Formulations for Incompressible Flow Computations, in: J. W. Hutchinson, T. Y. Wu (Eds.), Advances in Applied Mechanics, vol. 28 of *Advances in Applied Mechanics*, Elsevier, 1 – 44, 1992.

[23] T. J. Hughes, L. P. Franca, M. Balestra, A new finite element formulation for computational fluid dynamics: V. Circumventing the babuška-brezzi condition: a stable Petrov-Galerkin formulation of the stokes problem accommodating equal-order interpolations, Computer Methods in Applied Mechanics and Engineering 59 (1) (1986) 85 – 99.

[24] F. Brezzi, M. Fortin, Mixed and Hybrid Finite Element Methods, in: Vol. 15 of Springer Series in Computational Mathematics, Springer, New York, 1991.

[25] A. N. Brooks, T. J. Hughes, Streamline Upwind/Petrov-Galerkin formulations for convection dominated flows with particular emphasis on the incompressible Navier-Stokes equations, Comput. Methods Appl. Mech. Engrg. 32 (1-3) (1982) 199–259.

[26] T. E. Tezduyar, Computation of Moving Boundaries and Interfaces and Stabilization Parameters, International Journal for Numerical Methods in Fluids 43 (2003) 555–575, doi:10.1002/fld.505.

[27] M.-C. Hsu, Y. Bazilevs, V. Calo, T. Tezduyar, T. Hughes, Improving stability of stabilized and multiscale formulations in flow simulations at small time steps, Computer Methods in Applied Mechanics and Engineering 199 (13) (2010) 828 – 840, ISSN 0045-7825, doi:https://doi.org/10.1016/j.cma.2009.06.019, URL `http://www.sciencedirect.com/science/article/pii/S0045782509002254`, turbulence Modeling for Large Eddy Simulations.

[28] Y. Bazilevs, K. Takizawa, T. E. Tezduyar, Computational Fluid-Structure Interaction: Methods and Applications, John Wiley & Sons, Chichester, UK, 2013.

[29] H. Ben Dhia, Global-local approaches: the Arlequin framework, European Journal of Computational Mechanics 15 (1-3) (2006) 67–80.

[30] T. E. Tezduyar, Y. Osawa, Finite element stabilization parameters computed from element matrices and vectors, Computer Methods in Applied Mechanics and Engineering 190 (3) (2000) 411–430.

[31] S. Mittal, T. Tezduyar, Massively parallel finite element computation of incompressible flows involving fluid-body interactions, Computer Methods in Applied Mechanics and Engineering 112 (1) (1994) 253 – 282, ISSN 0045-7825.

[32] H. Schlichting (Deceased), K. Gersten, Boundary–Layer Equations in Plane Flow; Plate Boundary Layer, Springer Berlin Heidelberg, Berlin, Heidelberg, 145–164, 2017.

[33] U. Ghia, K. N. Ghia, C. T. Shin, High-Re solutions for incompressible flow using the Navier-Stokes equations and a multigrid method, Journal of Computational Physics 48 (1982) 387–441.

[34] M.-H. Wu, C.-Y. Wen, R.-H. Yen, M.-C. Weng, A.-B. Wang, Experimental and numerical study of the separation angle for flow around a circular cylinder at low Reynolds number, Journal of Fluid Mechanics 515 (2004) 233–260.

[35] H. Ding, C. Shu, K. S. Yeo, D. Xu, Simulation of incompressible viscous flows past a circular cylinder by hybrid FD scheme and meshless least square-based finite difference method, Comput. Methods Appl. Mech. Engrg. 193 (2004) 727–744.

[36] C. Liu, X. Zheng, C. Sung, Preconditioned Multigrid Methods for Unsteady Incompressible Flows, Journal of Computational Physics 139 (1) (1998) 35 – 57, ISSN 0021-9991, doi: https://doi.org/10.1006/jcph.1997.5859.

[37] L. Qu, C. Norberg, L. Davidson, S.-H. Peng, F. Wang, Quantitative numerical analysis of flow past a circular cylinder at Reynolds number between 50 and 200, Journal of Fluids and Structures 39 (2013) 347 – 370, ISSN 0889-9746, doi:https://doi.org/10.1016/j.jfluidstructs.2013.02.007.

[38] G. Weymouth, D. K. Yue, Boundary data immersion method for Cartesian-grid simulations of fluid-body interaction problems, Journal of Computational Physics 230 (16) (2011) 6233 – 6247, ISSN 0021-9991, doi:https://doi.org/10.1016/j.jcp.2011.04.022.

[39] T. Tezduyar, S. Aliabadi, M. Behr, S. Mittal, Massively parallel finite element simulation of compressible and incompressible flows, Computer Methods in Applied Mechanics and Engineering 119 (1) (1994) 157 – 177, ISSN 0045-7825, doi:https://doi.org/10.1016/0045-7825(94)00082-4.

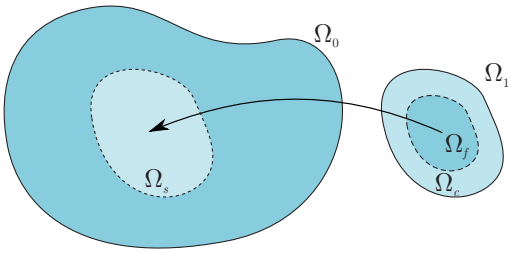


Figure 1: Model superposition in the Arlequin framework.

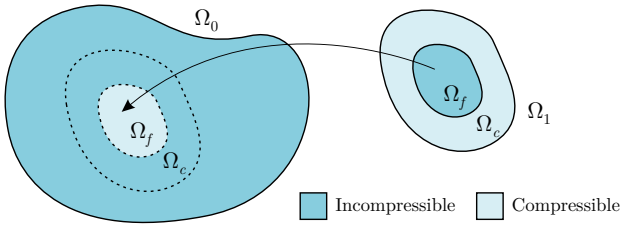


(a) Incompressibility contraint removed from local gluing zone.

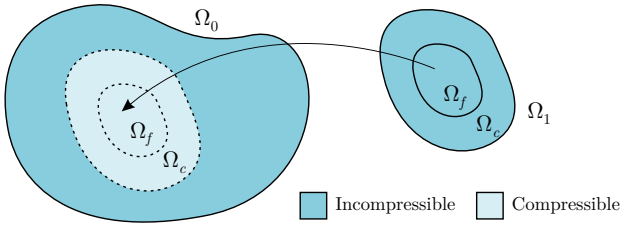


(b) Incompressibility constraint removed from global gluing zone.

Figure 2: Enforcement of the incompressibility constraint in the gluing zone $\Omega_c$.

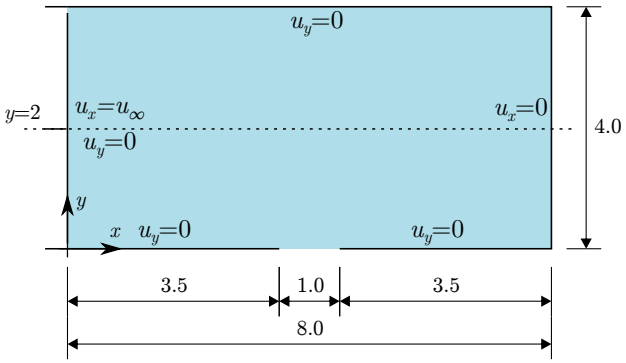


Figure 3: Pressurized fluid in a holed chamber: problem geometry and boundary conditions.

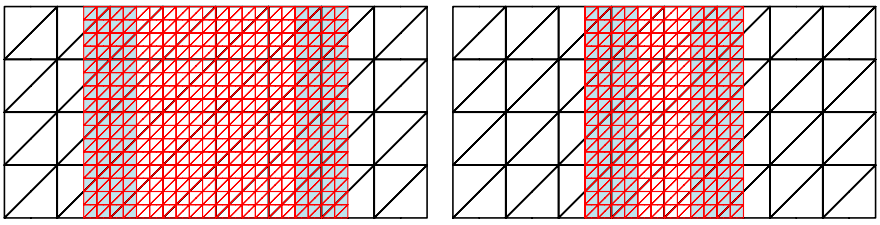

(a) Mesh 1. (b) Mesh 2.

Figure 4: Pressurized fluid in a holed chamber: global and local finite element models.

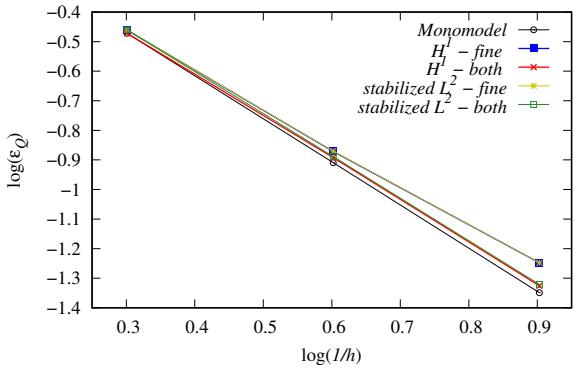


Figure 5: Pressurized fluid in a holed chamber: mass conservation convergence for monomodel, local model refinement $((H^1, L^2) - fine)$ and both models refinement $((H^1, L^2) - both)$.

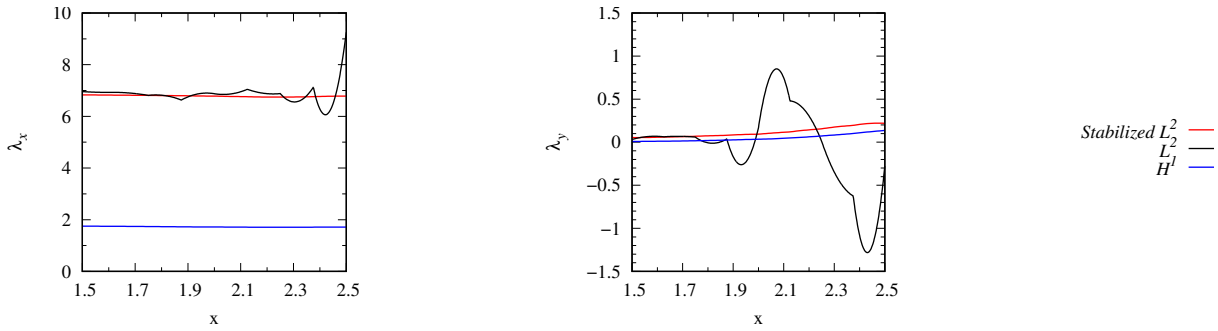


(a) (b)

Figure 6: Pressurized fluid in a holed chamber: Lagrange multiplier fields over the line $y = 2$.

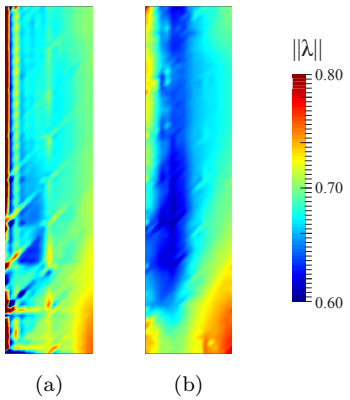


(a) (b)

Figure 7: Pressurized fluid in a holed chamber: Lagrange multiplier fields for (a) $L^2$ and (b) Stabilized $L^2$ coupling operators.

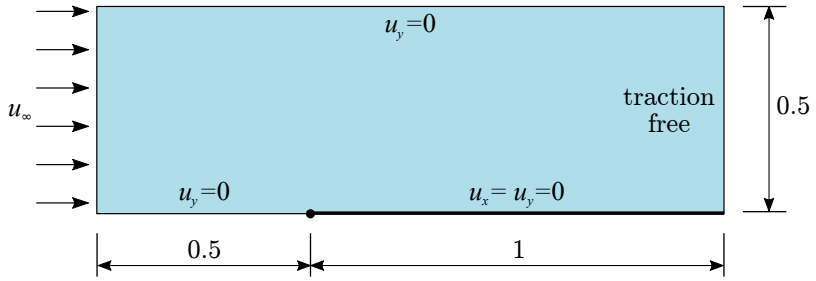


Figure 8: Flow over a flat plate: geometry and boundary conditions.

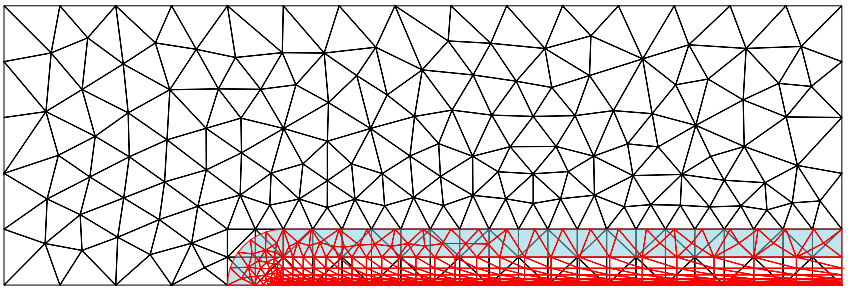

Figure 9: Flow over a flat plate: global and local finite element models.

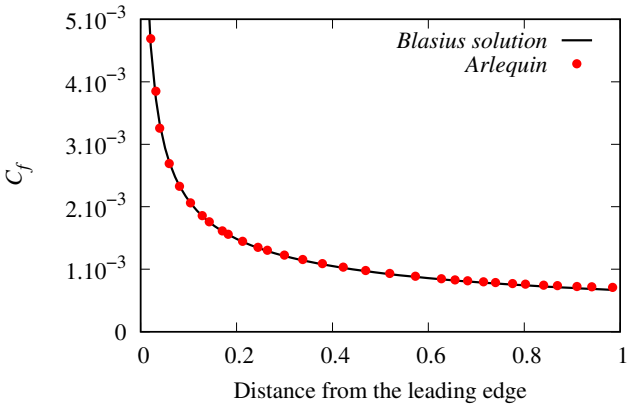


Figure 10: Flow over a flat plate: local skin friction coefficient along the flat plate.

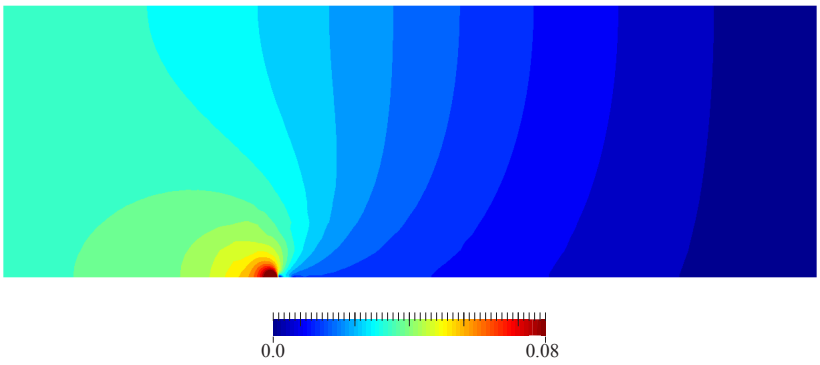


Figure 11: Flow over a flat plate: pressure field.

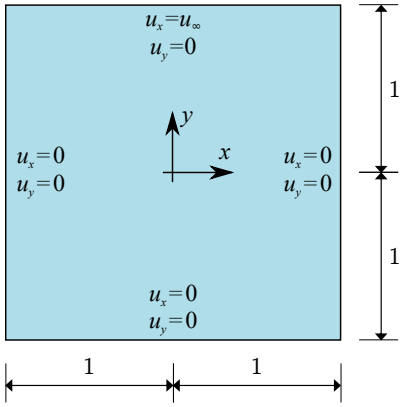


Figure 12: Square cavity flow: geometry and boundary conditions.

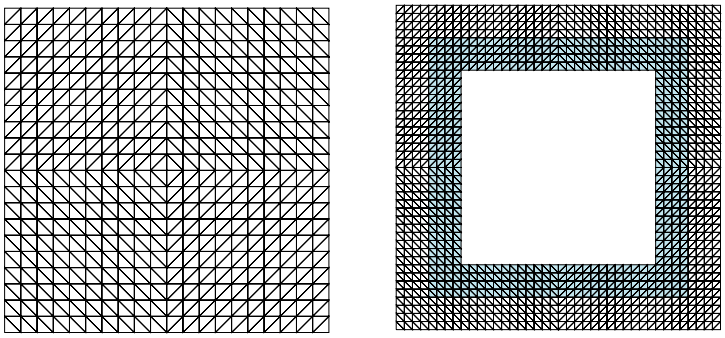

(a) Monomodel/Global model. (b) Local model.

Figure 13: Square cavity flow: global and local finite element models.

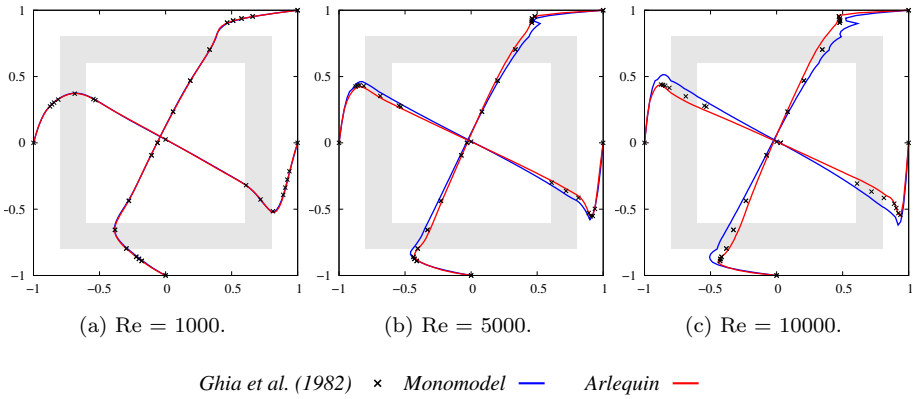


(a) Re = 1000. (b) Re = 5000. (c) Re = 10000.

Figure 14: Square cavity flow: velocity profiles for $u_x$ at $x = 0.5$ and for $u_y$ at $y = 0.5$.

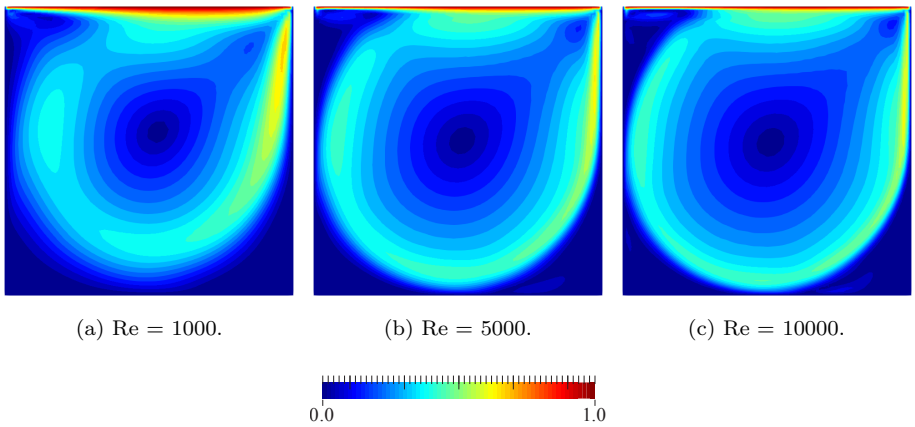


(a) Re = 1000. (b) Re = 5000. (c) Re = 10000.

Figure 15: Square cavity flow: Arlequin model velocity magnitude.

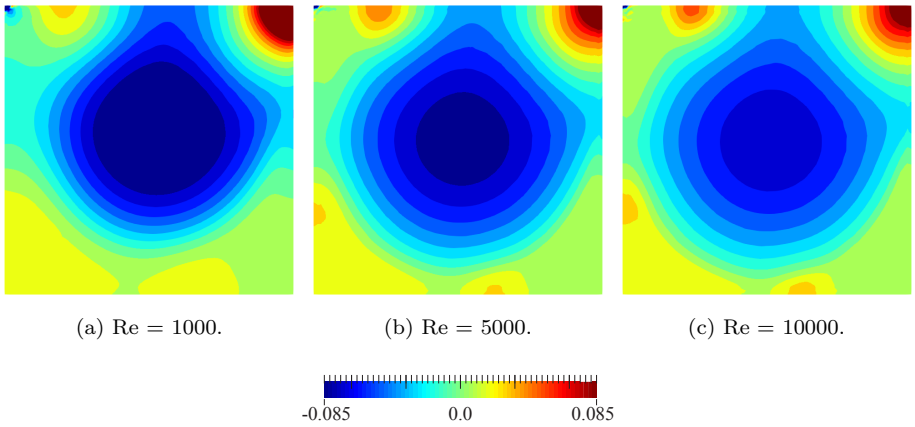


(a) Re = 1000. (b) Re = 5000. (c) Re = 10000.

Figure 16: Square cavity flow: Arlequin model pressure.

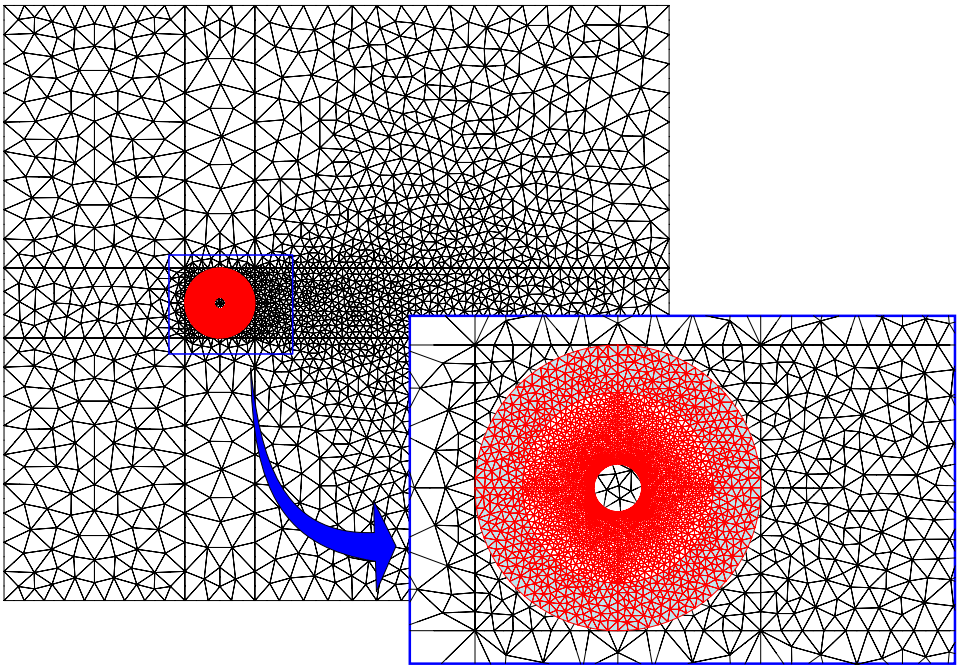

Figure 17: Flow over a circular cylinder: finite element global and fine models.

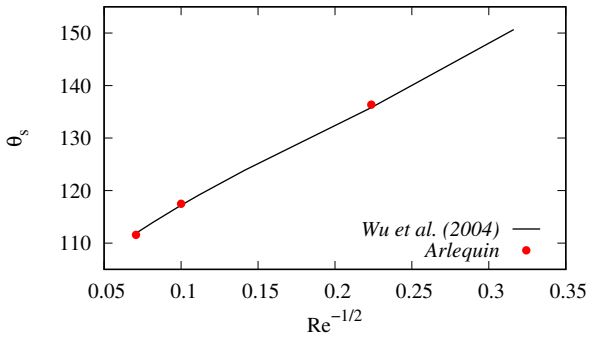


Figure 18: Flow over a circular cylinder: separation angle

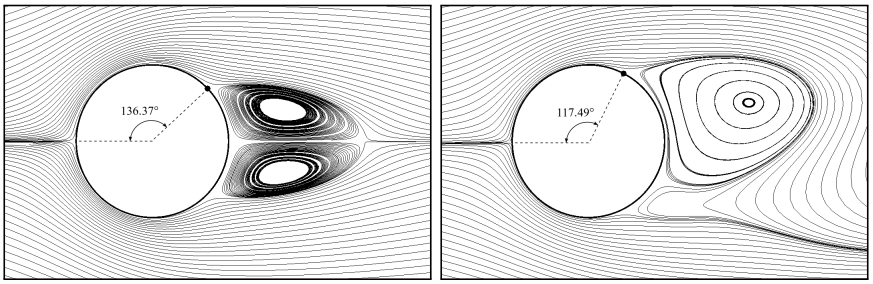


(a) Re = 20. (b) Re = 100.

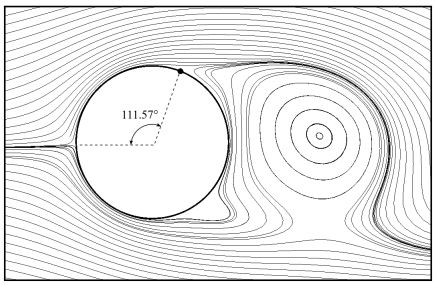


(c) Re = 200.

Figure 19: Flow over a circular cylinder: streamlines for the separation angle time-averaged values.

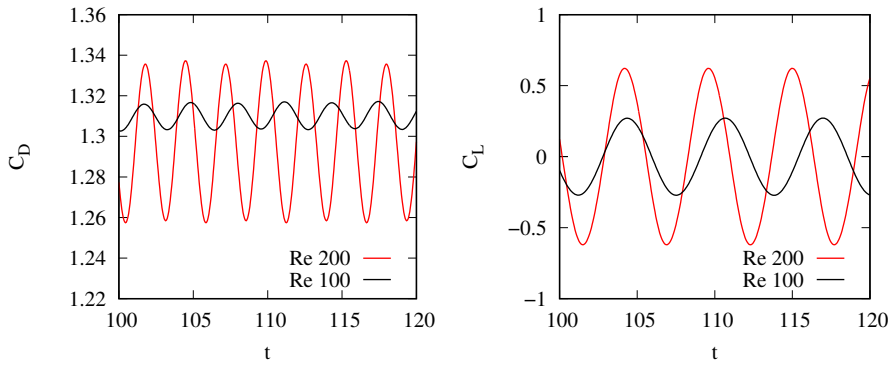


(a) Drag coefficient (b) Lift Coefficient

Figure 20: Flow over a circular cylinder: drag and lift coefficients.

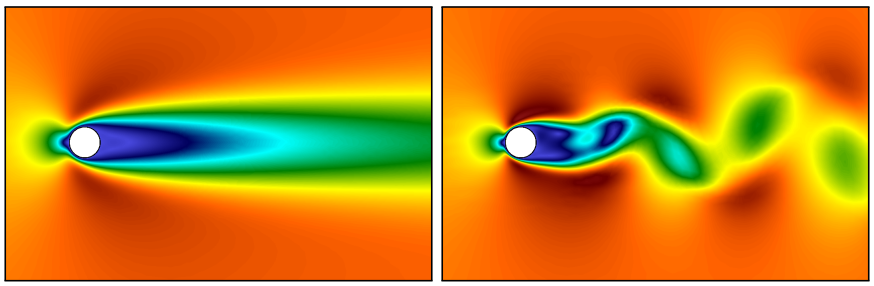

(a) Re = 20. (b) Re = 100.

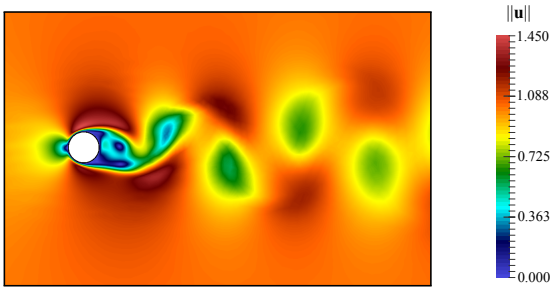


(c) Re = 200.

Figure 21: Flow over a circular cylinder: velocity magnitude for the separation angle time-averaged values.

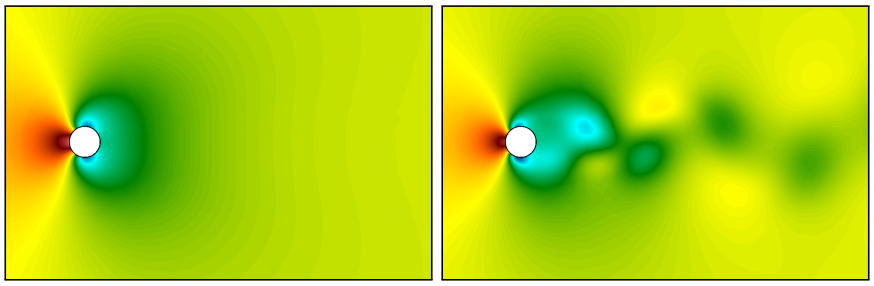

(a) Re = 20. (b) Re = 100.

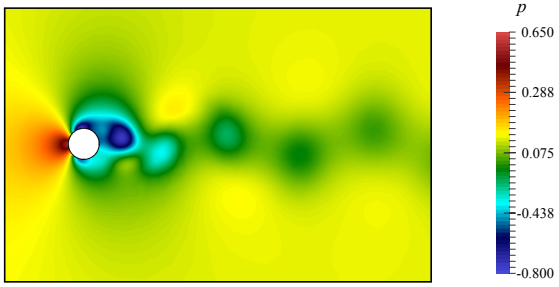


(c) Re = 200.

Figure 22: Flow over a circular cylinder: pressure fields for the separation angle time-averaged values.

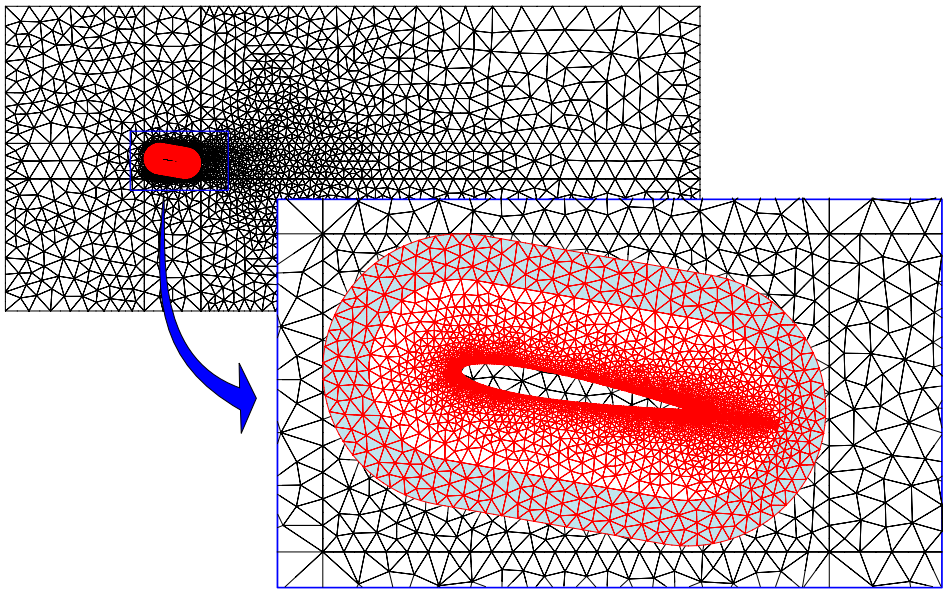

Figure 23: Flow past a stationary NACA 0012: finite element global and fine models.

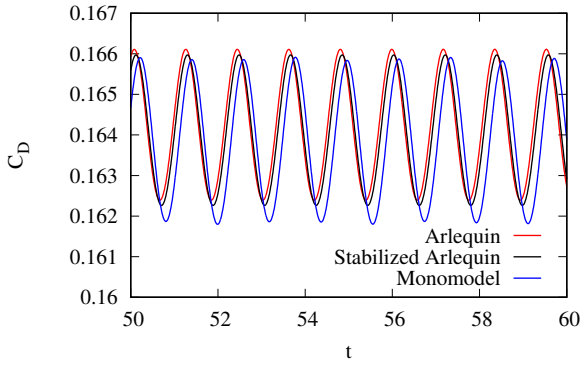


(a)

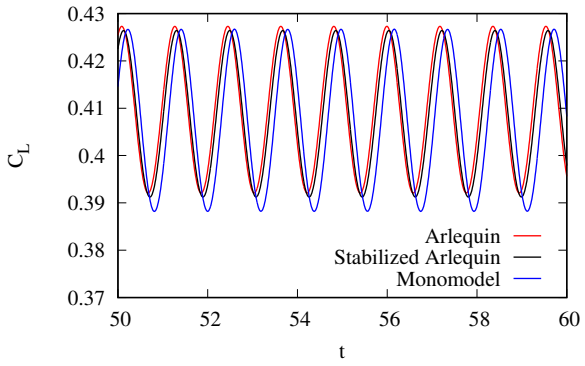


(b)

Figure 24: Flow past a stationary NACA 0012: time history for (a) drag and (b) lift coefficients.

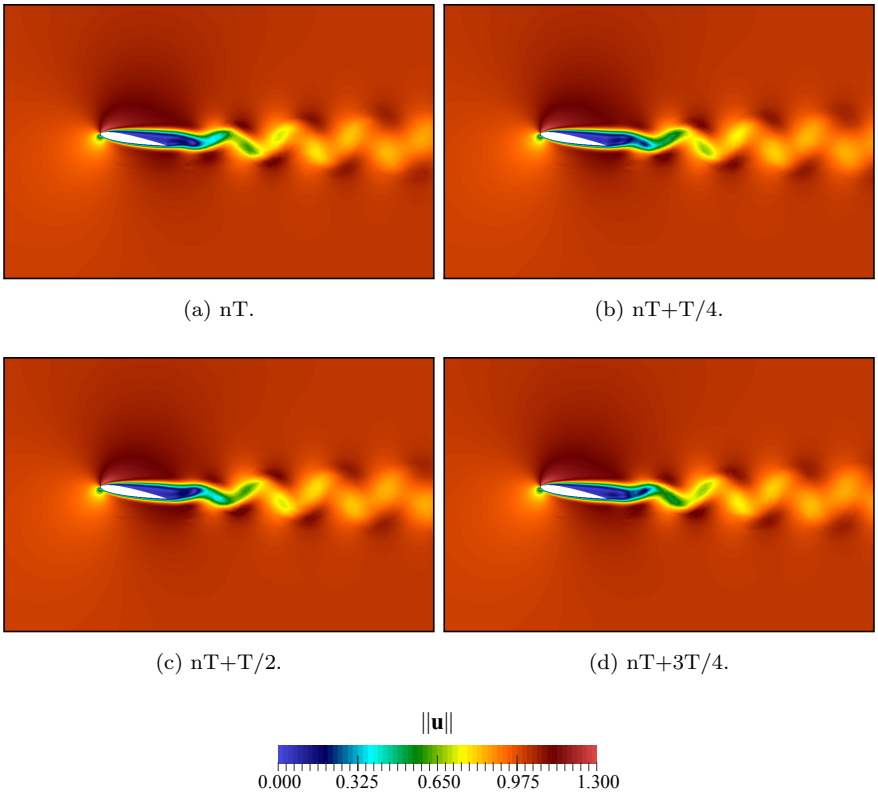


(a) nT. (b) nT+T/4.

(c) nT+T/2. (d) nT+3T/4.

Figure 25: Flow past a stationary NACA 0012: velocity magnitude for various time steps.

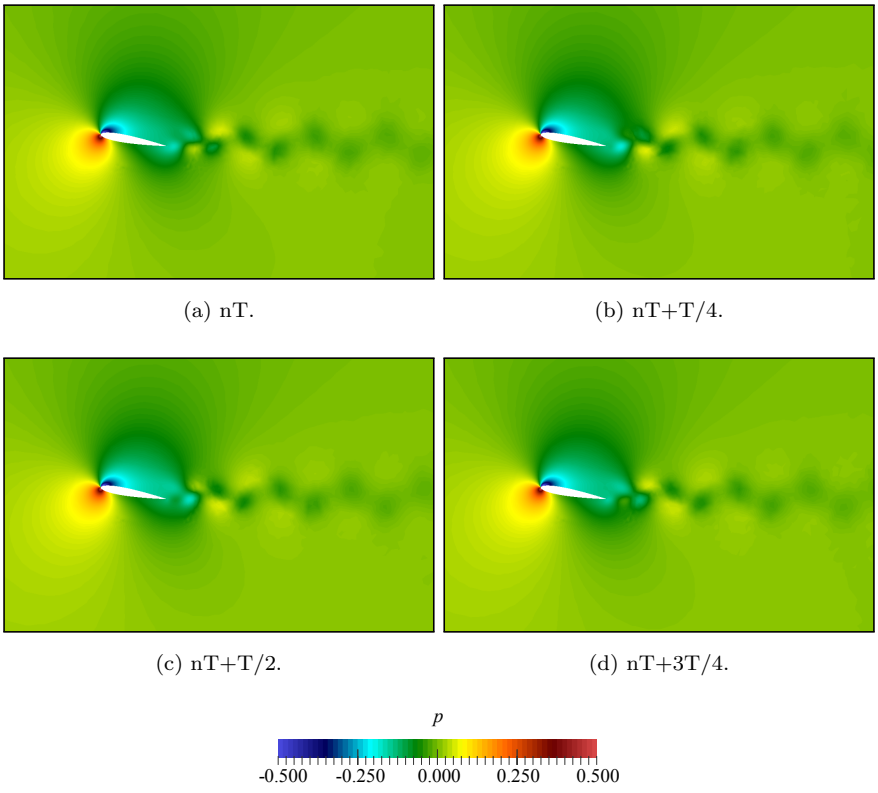


(a) nT. (b) nT+T/4.

(c) nT+T/2. (d) nT+3T/4.

Figure 26: Flow past a stationary NACA 0012: pressure field for various time steps.